

NEAR-INFRARED DETECTION OF WD 0806-661 B WITH THE *HUBBLE SPACE TELESCOPE*<sup>1</sup>K. L. LUHMAN<sup>2,3</sup>, C. V. MORLEY<sup>4</sup>, A. J. BURGASSER<sup>5</sup>, T. L. ESPLIN<sup>2</sup>, AND J. J. BOCHANSKI<sup>6</sup>*Draft version September 23, 2014*

## ABSTRACT

WD 0806-661 B is one of the coldest known brown dwarfs ( $T_{\text{eff}} = 300\text{--}345$  K) based on previous mid-infrared photometry from the *Spitzer Space Telescope*. In addition, it is a benchmark for testing theoretical models of brown dwarfs because its age and distance are well-constrained via its primary star ( $2\pm 0.5$  Gyr,  $19.2\pm 0.6$  pc). We present the first near-infrared detection of this object, which has been achieved through F110W imaging ( $\sim Y + J$ ) with the Wide Field Camera 3 on board the *Hubble Space Telescope*. We measure a Vega magnitude of  $m_{110} = 25.70 \pm 0.08$ , which implies  $J \sim 25.0$ . When combined with the *Spitzer* photometry, our estimate of  $J$  helps to better define the empirical sequence of the coldest brown dwarfs in  $M_{4.5}$  versus  $J - [4.5]$ . The positions of WD 0806-661 B and other Y dwarfs in that diagram are best matched by the cloudy models of Burrows et al. (2003) and the cloudless models of Saumon et al. (2012), both of which employ chemical equilibrium. The calculations by Morley et al. (2014) for 50% cloud coverage differ only modestly from the data. Spectroscopy would enable a more stringent test of the models, but based on our F110W measurement, such observations are currently possible only with *Hubble*, and would require at least  $\sim 10$  orbits to reach a signal-to-noise ratio of  $\sim 5$ .

*Subject headings:* binaries: visual — brown dwarfs — infrared: planetary systems — infrared: stars — planets and satellites: atmospheres

## 1. INTRODUCTION

Wide-field near-infrared (IR) imaging surveys have found hundreds of brown dwarfs in the solar neighborhood, reaching objects near the end of the T spectral sequence ( $T_{\text{eff}} > 500$  K, Burgasser et al. 2004; Warren et al. 2007; Delorme et al. 2008; Burningham et al. 2010; Lucas et al. 2010; Albert et al. 2011). Two members of the colder Y spectral class (Cushing et al. 2011) have been discovered as close companions to T dwarfs through near-IR adaptive optics imaging (Liu et al. 2011, 2012). However, because the near-IR fluxes of brown dwarfs collapse below  $\sim 400$  K (Burrows et al. 2003), space-based mid-IR telescopes offer the best sensitivity to Y dwarfs. Fortunately, two telescopes of this kind have been available in recent years, consisting of the *Spitzer Space Telescope* (Werner et al. 2004) and the *Wide-field Infrared Survey Explorer* (*WISE*, Wright et al. 2010). *Spitzer* imaging of fields surrounding nearby stars has uncovered a companion that is likely a Y dwarf (Luhman et al. 2011) and the all-sky map from *WISE* has found 19 free-

floating objects that are confirmed or likely Y dwarfs (Cushing et al. 2011, 2014; Kirkpatrick et al. 2012, 2013; Tinney et al. 2012; Luhman 2014; Pinfield et al. 2014). Following the initial mid-IR detections of Y dwarfs by these satellites, further characterization of their spectral energy distributions is currently possible only through deep photometry or spectroscopy at near-IR wavelengths (Leggett et al. 2013; Cushing et al. 2014).

The probable Y dwarf discovered with *Spitzer* is a companion to the white dwarf WD 0806-661. It has an estimated mass of  $6\text{--}9 M_{\text{Jup}}$  (Luhman et al. 2012) and a projected separation of  $130''$ , corresponding to 2500 AU at the distance of the primary ( $19.2\pm 0.6$  pc, Subasavage et al. 2009). WD 0806-661 B has not been classified spectroscopically, but it is likely to have a Y spectral type since it is less luminous than most confirmed Y dwarfs (Luhman et al. 2012; Marsh et al. 2013; Dupuy & Kraus 2013; Beichman et al. 2014). In addition to being one of the coldest known brown dwarfs ( $T_{\text{eff}} = 300\text{--}345$  K, Luhman et al. 2012), WD 0806-661 B was the first Y dwarf with an accurate distance because of its companionship to a star with a previously measured parallax, and it is the only Y dwarf with a well-constrained age because its primary is a white dwarf. As a result, it represents a unique benchmark for testing atmospheric and evolutionary models of substellar objects at very low temperatures. However, because of its large distance compared to other known Y dwarfs, WD 0806-661 B is particularly faint and few data are available for comparison to models; it has been detected in only the 3.6 and  $4.5 \mu\text{m}$  bands of *Spitzer* to date and has a rather faint limit on its near-IR flux ( $J > 23.9$ , Luhman et al. 2012).

In pursuit of the first near-IR detection of WD 0806-661 B, we have obtained images of it with the Wide Field Camera 3 (WFC3) on board the *Hubble Space Telescope*

<sup>1</sup> Based on observations made with the NASA/ESA *Hubble Space Telescope* through program 12815, obtained at the Space Telescope Science Institute, which is operated by the Association of Universities for Research in Astronomy, Inc., under NASA contract NAS 5-26555, and observations with the ESO Telescopes at Paranal Observatory under programs ID 089.C-0428 and ID 089.C-0597.

<sup>2</sup> Department of Astronomy and Astrophysics, The Pennsylvania State University, University Park, PA 16802, USA; kluhman@astro.psu.edu

<sup>3</sup> Center for Exoplanets and Habitable Worlds, The Pennsylvania State University, University Park, PA 16802, USA

<sup>4</sup> Department of Astronomy and Astrophysics, University of California, Santa Cruz, CA 95064, USA

<sup>5</sup> Center for Astrophysics and Space Science, University of California San Diego, La Jolla, CA 92093, USA

<sup>6</sup> Haverford College, 370 Lancaster Avenue, Haverford, PA 19041, USA

(*HST*), which is the most sensitive near-IR camera that is currently available. We have also analyzed archival images of WD 0806-661 B from the Very Large Telescope (VLT). In this paper, we describe the collection and reduction of these data (Section 2) and use the reduced images to constrain the binarity of WD 0806-661 B, refine the empirical sequence of Y dwarfs in a color-magnitude diagram, and test models of brown dwarfs (Section 3). We conclude by placing our near-IR data for WD 0806-661 B in the context of other known Y dwarfs and discussing additional observations that would further constrain the models (Section 4).

## 2. OBSERVATIONS

### 2.1. F110W Images from *HST*

We obtained images of WD 0806-661 B with the IR channel of WFC3 (Kimble et al. 2008) on 2013 February 8 and 9 (UT). The camera contains a  $1024 \times 1024$  HgCdTe array in which the pixels have dimensions of  $\sim 0''.135 \times 0''.121$ . The inner  $1014 \times 1014$  portion of the array detects light, which corresponds to a field of view of  $136'' \times 123''$ . We selected the F110W filter for these observations because it appeared to offer the best sensitivity to cold brown dwarfs among the available WFC3 filters based on simulations with the instrument's exposure time calculator using spectra of late T dwarfs. This filter spans from  $\sim 0.9\text{--}1.4\ \mu\text{m}$ , corresponding roughly to the sum of the *Y* and *J* filters. The observations were performed during three identical two-orbit visits. In a given orbit, one 1003 s exposure was collected at each position in a three-point dither pattern. The dither patterns in the two orbits in each visit were offset by 3.5 pixels along the x-axis of the array.

The 18 WFC3 images were registered and combined using the tasks *tweakreg* and *astrodrizzle* within the DrizzlePac software package. We adopted a drop size of 0.85 native pixels and a resampled plate scale of  $0''.065\ \text{pixel}^{-1}$ . Point sources in the reduced image exhibit  $\text{FWHM} \sim 0''.18$ . We aligned the world coordinate system of the WFC3 image to that of the IRAC images from Luhman et al. (2011, 2012) using offsets in right ascension, declination, and rotation that were derived from sources detected by both WFC3 and IRAC. In Figure 1, we present a small portion of the WFC3 image surrounding the positions of WD 0806-661 B in the IRAC images, which were taken in 2004 and 2009. We have estimated the location of WD 0806-661 B on the date of the WFC3 observation by combining the astrometry from IRAC with the proper motion and parallax of the primary (Subasavage et al. 2009). As shown in Figure 1, a source is detected in the WFC3 image at  $\sim 1\ \sigma$  from the expected position, which we take to be WD 0806-661 B.

Aperture photometry was measured for WD 0806-661 B using an aperture radius of  $0''.26$  and radii of  $0''.26$  and  $0''.65$  for the inner and outer boundaries of the sky annulus, respectively. We converted that measurement to an aperture radius of  $0''.4$  using an aperture correction of 0.097 mag, which was estimated from well-detected, isolated stars in the image. We then applied the zero-point Vega magnitude for F110W for an aperture radius of  $0''.4$ , which is 25.8829<sup>7</sup>. The resulting F110W photometry is given in Table 1.

### 2.2. *z* and *Y* Images from VLT

To further constrain the spectral energy distribution of WD 0806-661 B, we have made use of unpublished images in the *z* and *Y* bands that are publicly available in the data archive of the VLT. The *z*-band images were collected with the Focal Reducer/Low Dispersion Spectrograph 2 (Appenzeller et al. 1998) on the VLT Unit Telescope 1 on the night of 2012 March 30 (P. Delorme, ID 089.C-0597). The camera contains two  $2048 \times 4096$  CCDs. The observations were performed with the Standard Resolution collimator and  $2 \times 2$  binning, which produced a plate scale of  $0''.25\ \text{pixel}^{-1}$ . WD 0806-661 B was placed within one array and 38 dithered images were taken, each with an exposure time of 120 s. We bias subtracted and flat fielded the individual frames, and registered and combined them into a single mosaic. The FWHM of point sources in the combined image was  $\sim 0''.7$ . The image was flux calibrated using photometry in *z*(AB) for a calibration star, G138-31, from the Ninth Data Release of the Sloan Digital Sky Survey Photometric Catalog (Ahn et al. 2012) combined with a conversion from *z*(AB) to *z*(Vega)<sup>8</sup>.

The *Y*-band images were obtained with the High Acuity Wide-Field K-band Imager (Kissler-Patig et al. 2008) on the VLT Unit Telescope 4 on the night of 2012 May 21 (M. Burleigh, ID 089.C-0428). The camera contains four  $2048 \times 2048$  HgCdTe arrays and has a plate scale of  $0''.106\ \text{pixel}^{-1}$ . WD 0806-661 B was placed within one of the four arrays and 28 dithered images were taken, each consisting of 26 coadded 2 s exposures. Following dark subtraction and flat fielding, the images were registered and combined. Point sources in the combined image had  $\text{FWHM} \sim 0''.6$ . Stars in the observed field exhibited significant flux variations ( $\sim 0.4$  mag) among the dithered frames, indicating that the conditions were not photometric and that the photometric standard star probably would not provide an accurate flux calibration. For stars appearing in our *z* and F110W images and the previous *J*-band images from Luhman et al. (2012), the median values of  $z - m_{110}$  and  $m_{110} - J$  differ by  $\sim 0.2$  mag; the difference in the medians of  $Y - m_{110}$  and  $m_{110} - J$  should be even smaller because of the smaller wavelength range spanned. Therefore, we performed a rough calibration of the *Y*-band image by requiring that  $Y - m_{110}$  and  $m_{110} - J$  have the same medians.

We find that WD 0806-661 B is not detected in the *z* and *Y* images. The magnitude limits that correspond to a signal-to-noise ratio (S/N) of 3 are provided in Table 1.

## 3. ANALYSIS

### 3.1. Multiplicity Constraints

We searched for binary companions to WD 0806-661 B in the drizzle-combined F110W image through a point source function (PSF) fitting algorithm. An empirical PSF was constructed by median-combining normalized and background-subtracted  $1''.4 \times 1''.4$  subimages of 96 high S/N ( $>50$ ), unsaturated, normalized point sources in the drizzled frame. This PSF may not precisely represent those of WD 0806-661 B or a cooler companion due to the significantly different spectral energy distributions of the field stars; however, this is our best option given

<sup>7</sup> [http://www.stsci.edu/hst/wfc3/phot\\_zp\\_lbn](http://www.stsci.edu/hst/wfc3/phot_zp_lbn)

<sup>8</sup> <http://www.sdss.org/dr7/algorithms/sdssUBVRITransform.html>

the necessity of using the drizzle-combined image. An alternate method, using Tiny Tim PSF models (Krist 1995), is also not feasible as this code is currently not set up for subsampled WFC3 images. We fit both single and binary PSF models to a comparably-sized subimage centered on WD 0806-661 B using a Monte Carlo Markov Chain algorithm with  $\chi^2$  evaluation to determine the optimal primary and secondary  $x$  and  $y$  pixel positions and fluxes. The binary model failed to provide a significantly better fit ( $>90\%$  confidence) to the data based on an F-test analysis, so we rule out detection of a companion. We assessed our sensitivity limit by performing an identical series of binary fits to 10,000 simulated subimages with companion PSFs implanted, sampling  $0 < \Delta m_{110} < 3$ , separations of 1 to 8.5 pixels ( $0''.065$ – $0''.553$ ) and all position angles. Fits were deemed successful if the recovered companion had a separation and relative magnitude within 0.5 pixels and 0.3 mag of the input parameters. Figure 2 displays the 20%, 50% and 80% recovery limits as a function of separation and relative magnitude ( $\Delta m_{110}$ ). Beyond  $0''.13$ , the 50% (80%) limit is  $\Delta m_{110} \sim 0.9$  mag ( $\sim 0.7$  mag), which corresponds to  $\Delta T_{\text{eff}} \sim 15$  K based on the models of brown dwarfs described in Section 3.2.1. These limits were verified by visual examination of the implanted companions.

### 3.2. Comparison of Observed and Model Photometry

#### 3.2.1. Y Dwarf Models Selected for Comparison

For comparison to the data for WD 0806-661 B, we have considered four sets of models for the spectral energy distributions of Y dwarfs that are characterized primarily by the following features: water clouds and chemical equilibrium (Burrows et al. 2003), cloudless and chemical equilibrium (Saumon & Marley 2008; Saumon et al. 2012), cloudless and non-equilibrium chemistry (Saumon & Marley 2008; Saumon et al. 2012), and 50% coverage of water, chloride, and sulfide clouds and chemical equilibrium (Morley et al. 2012, 2014). These models have been previously compared to color-magnitude diagrams of late T and Y dwarfs, the results of which can be summarized as follows:  $Y - J$  is better matched by the cloudless models while the cloudy models predict colors that are too red (Liu et al. 2012; Leggett et al. 2013; Morley et al. 2014). The opposite is true for  $J - H$ , which is reproduced by the cloudy models of Morley et al. (2012, 2014) while the cloudless model colors are too blue (Morley et al. 2012, 2014; Leggett et al. 2013; Marsh et al. 2013; Beichman et al. 2014). The values of  $H - K$  predicted by both cloudy and cloudless models are too blue, possibly because of incomplete methane line lists (Morley et al. 2014). The mid-IR bands that have been considered consist of the 3.4, 4.6, and 12  $\mu\text{m}$  bands from *WISE* (*W1*, *W2*, and *W3*) and the 3.6 and 4.5  $\mu\text{m}$  bands from *Spitzer* ([3.6] and [4.5]). Both the cloudy and cloudless models are roughly consistent with previous data for Y dwarfs in color-magnitude diagrams composed of [4.5] or *W2* and colors spanning from those bands to  $J$ ,  $H$ , and *W3* (Leggett et al. 2013; Morley et al. 2014), although the large scatter in the data precludes discrimination between the models. Finally, both sets of model colors are too red in color-magnitude diagrams involving [3.6]–[4.5] (Leggett et al. 2010; Luhman et al. 2012; Beichman et al. 2014).

#### 3.2.2. Color-Magnitude Diagrams

The previous photometry and our new measurements for WD 0806-661 B are compiled in Table 1. We wish to use our new data to test the models of Y dwarfs described in the previous section. Before doing so, we would like to convert  $m_{110}$  to  $J$  since it is more widely available for other Y dwarfs and is encompassed by the F110W filter. To perform this conversion, we have computed  $m_{110} - J$  from observed and model spectra of cold brown dwarfs using the transmission profiles of F110W and  $J$  on the Mauna Kea Observatories Near-Infrared system (Simons & Tokunaga 2002; Tokunaga et al. 2002; Tokunaga & Vacca 2005). For the observed spectra, we have considered the published spectra of dwarfs later than T8 that fully span the wavelength range of F110W and that have the highest S/N, which corresponds to the data for UGPS J072227.51-054031.2 (T9), WISEPC J014807.25-720258.8 (T9.5), and WISEP J154151.65-225025.2 (Y0.5) from Cushing et al. (2011). These spectra exhibit  $m_{110} - J = 0.88$ , 0.87, and 0.65, respectively. Meanwhile, the models that are near the value of  $M_{4.5}$  for WD 0806-661 B (similar to that of WISEP J154151.65-225025.2) produce  $m_{110} - J$  colors of 1.2 (Burrows et al. 2003), 0.66 (chemical equilibrium) and 0.81 (non-equilibrium) (Saumon et al. 2012), and 0.75 (Morley et al. 2014). We ignore the color from Burrows et al. (2003) since it is significantly redder than the data for T/Y dwarfs (a similar difference is present in  $Y - J$ , Liu et al. 2012). The remaining model colors are roughly similar to the observed values. These observed and model colors suggest that WD 0806-661 B probably has  $m_{110} - J \sim 0.7$ , which implies  $J \sim 25.0$  when combined with our measurement of  $m_{110}$ .

We can derive new constraints on the colors of WD 0806-661 B by combining our estimate of  $J$ , the limits on  $z$  and  $Y$ , and the existing photometry in [4.5]. These data produce  $z - J > -0.4$ ,  $Y - J > -1.8$ , and  $J - [4.5] \sim 8.1$ . For the first two colors, most previous measurements for Y dwarfs range from  $z - J = 2.2$  to 3.2 (with Vega  $z$ ) and from  $Y - J = -0.5$  to 0.4 (Liu et al. 2012; Leggett et al. 2013; Lodieu et al. 2013). Thus, the  $z$  and  $Y$  data are not sufficiently deep to provide useful constraints on those colors. To make use of  $J - [4.5]$ , we plot WD 0806-661 B on a diagram of  $M_{4.5}$  versus  $J - [4.5]$  in Figure 3. We choose  $M_{4.5}$  as the magnitude since this band encompasses less atmospheric absorption and usually has the smallest photometric errors among the broad-band filters in which Y dwarfs have been observed. WD 0806-661 B is also shown on a diagram of  $M_{4.5}$  versus [3.6]–[4.5] in Figure 4. In both diagrams, we include a sample of T dwarfs (Dupuy & Liu 2012) and all other known Y dwarfs that have photometry in these bands and parallax measurements (Cushing et al. 2011, 2014; Tinney et al. 2012; Beichman et al. 2013, 2014; Leggett et al. 2013; Marsh et al. 2013; Kirkpatrick et al. 2013; Dupuy & Kraus 2013; Luhman 2014). The data are shown separately with each of the four sets of Y dwarf models that we are considering (Section 3.2.1) for ages of 1 and 3 Gyr, which bracket the age of WD 0806-661 ( $2 \pm 0.5$  Gyr, Luhman et al. 2012). In the diagram of  $M_{4.5}$  versus  $J - [4.5]$  for a given set of models,  $J$  for WD 0806-661 B has been estimated by combining our measurement of  $m_{110}$  with the value of  $m_{110} - J$  predicted by those

models at the  $4.5 \mu\text{m}$  absolute magnitude of WD 0806-661 B. Thus, the relative positions of WD 0806-661 B and the models in that diagram are as they would be in a diagram of  $M_{4.5}$  versus  $m_{110} - [4.5]$ .

The Y dwarfs in  $M_{4.5}$  versus  $J - [4.5]$  in Figure 3 exhibit significant scatter, but the data have reached sufficient quality that a recognizable sequence is becoming apparent among a subset of Y dwarfs. This sequence consists of the five Y dwarfs at  $J - [4.5] \sim 5-6$ , the four Y dwarfs at  $J - [4.5] \sim 7-8$ , and WD 0806-661 B. The vertical dispersion among these objects is similar to that of the T dwarf sequence. The scatter in  $M_{4.5}$  versus  $[3.6] - [4.5]$  is smaller and the Y dwarf sequence is better defined, as shown in Figure 4. WISE J014656.66+423410.0 is a moderate outlier in  $M_{4.5}$  versus  $J - [4.5]$  (the bluest Y dwarf), but it is within the sequence of other Y dwarfs in  $M_{4.5}$  versus  $[3.6] - [4.5]$ . WISE J035934.06-540154.6 falls below the Y dwarf sequence in both diagrams. WISE J071322.55-291751.9 and WISE J140518.40+553421.5 appear to be overluminous in each diagram to a degree that is consistent with unresolved binaries. WISE J182831.08+265037.8 is also brighter than both sequences, although the difference in  $M_{4.5}$  versus  $J - [4.5]$  is too large to be explained through binarity alone. The anomalous photometric properties of this object have been discussed previously (Beichman et al. 2013; Leggett et al. 2013). WD 0806-661 B does not appear to be overluminous in either color-magnitude diagram, indicating that it is probably not an unresolved binary in which the components have similar fluxes.

In Figures 3 and 4, the Y dwarf isochrones at 1 and 3 Gyr from Burrows et al. (2003) differ only modestly; the isochrones for these ages are quite similar to each other for each of the remaining three sets of models. Because the model isochrones do not vary significantly with age, we can compare them to both WD 0806-661 B and the Y dwarf population as a whole. In  $M_{4.5}$  versus  $J - [4.5]$ , the cloudy models of Burrows et al. (2003) and the cloudless models of Saumon et al. (2012) agree fairly well with WD 0806-661 B and the Y dwarf sequence. The cloudy models of Morley et al. (2014) are slightly bluer than those data at fainter magnitudes, and the non-equilibrium models of Saumon et al. (2012) are bluer still. In  $M_{4.5}$  versus  $[3.6] - [4.5]$ , all of the models are significantly redder than the data, which has been noticed previously for T and Y dwarfs (Leggett et al. 2010; Beichman et al. 2014). Given that the models resemble the data in  $M_{4.5}$  versus  $J - [4.5]$  but not  $M_{4.5}$  versus  $[3.6] - [4.5]$ , this discrepancy may be primarily due to errors in the predicted  $3.6 \mu\text{m}$  fluxes, although near- and mid-IR spectroscopy are needed for a definitive conclusion.

#### 4. DISCUSSION

Through imaging with WFC3 on *HST*, we have obtained the first near-IR detection of the coldest known benchmark brown dwarf, WD 0806-661 B. We have measured  $m_{110} = 25.7$ , from which we estimate  $J \sim 25.0$ . When combined with previous *Spitzer* photometry, these data produce  $J - [4.5] \sim 8.1$ , which makes WD 0806-661 B approximately the fourth reddest known Y dwarf in that color. WD 0806-661 B also could be compared to other Y dwarfs in terms of  $M_J$  to constrain their rel-

ative temperatures, although that is better done with the more accurate photometry that has been measured at  $4.5 \mu\text{m}$  for most Y dwarfs. However, mid-IR photometry is unavailable for two Y dwarfs because they are close companions, consisting of CFBDSIR J1458+1013 B and WISEPC J121756.91+162640.2 B (Liu et al. 2011, 2012). WD 0806-661 B is  $\sim 30$  times fainter than those objects in  $M_J$ , which indicates that it is  $\sim 100$  K colder based on models of Y dwarfs. In  $J - [4.5]$  versus  $M_{4.5}$ , WD 0806-661 B has a relatively well-constrained position that helps to solidify an empirical sequence of Y dwarfs that has recently begun to emerge.

We have compared the sequence produced by WD 0806-661 B and other Y dwarfs in  $J - [4.5]$  versus  $M_{4.5}$  to the predictions of theoretical models. The cloudy models of Burrows et al. (2003) and the cloudless models of Saumon et al. (2012) provide the best agreement with the data, although only modest differences are present with the cloudy models of Morley et al. (2014). Based on these results and previous comparisons in other color-magnitude diagrams (e.g., Leggett et al. 2013; Morley et al. 2014), no single set of models produces a clearly superior fit to the spectral energy distributions of Y dwarfs at this time. According to Saumon et al. (2012) and Morley et al. (2014), the differences in the  $J - [4.5]$  colors for cloudy and cloudless atmospheres increase with fainter magnitudes. Thus, measurements of  $J - [4.5]$  for the few known Y dwarfs that are less luminous than WD 0806-661 B would help to discriminate between those models. For instance, WISE J085510.83-071442.5 is the coldest known brown dwarf ( $T_{\text{eff}} \sim 250$  K) and has not been detected at near-IR wavelengths ( $J > 23$ , Luhman 2014). The cloudy and cloudless models of Saumon et al. (2012) and Morley et al. (2014) predict that it should have  $J - 4.5 \sim 10.3$  and  $12.7$ , corresponding to  $J \sim 24.2$  and  $26.6$ , respectively. Other commonly considered colors like  $Y - J$  and  $J - H$  do not differ significantly between those models for the coldest Y dwarfs (Morley et al. 2014), but measurements of these colors for WD 0806-661 B and colder objects nevertheless would be useful for further constraining the models in general.

Spectroscopy of WD 0806-661 B will be necessary in order to fully exploit its potential as a benchmark for testing model atmospheres. Our near-IR photometry indicates that it is too faint for spectroscopy with existing ground-based telescopes. WFC3 on *HST* is the only available spectrograph that is capable of detecting it. Based on previous WFC3 observations of Y dwarfs (Cushing et al. 2011, 2014; Kirkpatrick et al. 2012, 2013), a minimum of  $\sim 10$  orbits would be required to reach  $S/N \sim 5$  in low-resolution near-IR spectroscopy of WD 0806-661 B. Because they will offer greater near-IR sensitivity than *HST* and will extend to mid-IR wavelengths, the next generation of 20-40 m ground-based telescopes and the *James Webb Space Telescope* will enable detailed characterization of the spectra of WD 0806-661 B and other Y dwarfs and discrimination among the competing models of their atmospheres (Morley et al. 2014).

We acknowledge support from grant GO-12815 from the Space Telescope Science Institute. The Center for

TABLE 1  
PHOTOMETRY OF WD 0806-661 B

Band	Magnitude	Reference
<i>z</i>	>24.6	1
<i>Y</i>	>23.2	1
<i>m</i> <sub>110</sub>	25.70±0.08	1
<i>J</i>	>23.9	2
<i>J</i> 3	>23.5	2
[3.6]	19.65±0.15	2
[4.5] (2004)	16.96±0.09	2
[4.5] (2009)	16.84±0.06	2
[4.5] (mean)	16.88±0.05	2

REFERENCES. — (1) this work; (2) Luhman et al. (2012).

NOTE. — All data are Vega magnitudes. The limits correspond to  $S/N > 3$ . Observed and model spectra of Y dwarfs imply  $m_{110} - J \sim 0.7$  (Section 3.2.2).

Exoplanets and Habitable Worlds is supported by the

Pennsylvania State University, the Eberly College of Science, and the Pennsylvania Space Grant Consortium.

#### REFERENCES

- Ahn, C. P., Alexandroff, R., Allende Prieto, C., et al. 2012, *ApJS*, 203, 21
- Albert, L., Étienne, A., Delorme, P., et al. 2011, *AJ*, 141, 203
- Appenzeller, I., Fricke, K., Furtig, W., et al. 1998, *The Messenger*, 94, 1
- Beichman, C., Gelino, C. R., Kirkpatrick, J. D., et al. 2013, *ApJ*, 764, 101
- Beichman, C., Gelino, C. R., Kirkpatrick, J. D., et al. 2014, *ApJ*, 783, 68
- Burgasser, A. J., McElwain, M. W., Kirkpatrick, J. D., et al. 2004, *AJ*, 127, 2856
- Burningham, B., Pinfield, D. J., Lucas, P. W., et al. 2010, *MNRAS*, 406, 1885
- Burrows, A., Sudarsky, D., & Lunine, J. I. 2003, *ApJ*, 596, 587
- Cushing, M. C., Kirkpatrick, J. D., Gelino, C. R., et al. 2011, *ApJ*, 743, 50
- Cushing, M. C., Kirkpatrick, J. D., Gelino, C. R., et al. 2014, *AJ*, 147, 113
- Delorme, P., Delfosse, X., Albert, L., et al. 2008, *A&A*, 482, 961
- Dupuy, T. J., & Kraus, A. L. 2013, *Science*, 341, 1492
- Dupuy, T. J., & Liu, M. C. 2012, *ApJS*, 201, 19
- Kimble, R. A., MacKenty, J. W., O’Connell, R. W., & Townsend, J. A. 2008, *Proc. SPIE*, 7010, 43
- Kirkpatrick, J. D., Cushing, M. C., Gelino, C. R., et al. 2013, *ApJ*, 776, 128
- Kirkpatrick, J. D., Gelino, C. R., Cushing, M. C., et al. 2012, *ApJ*, 753, 156
- Kissler-Patig, M., Pirard, J.-F., Casali, M., et al. 2008, *A&A*, 491, 941
- Krist, J. 1995, *ASP Conf. Ser. 77, Astronomical Data Analysis Software and Systems IV*, ed. R.A. Shaw, H.E. Payne, & J.J.E. Hayes (San Francisco, CA: ASP), 349
- Leggett, S. K., Burningham, B., Saumon, D., et al. 2010, *ApJ*, 710, 1627
- Leggett, S. K., Morley, C. V., Marley, M. S., et al. 2013, *ApJ*, 763, 130
- Liu, M. C., Deacon, N. R., Magnier, E. A., et al. 2011, *ApJ*, 740, 108
- Liu, M. C., Dupuy, T. J., Bowler, B. P., Leggett, S. K., & Best, W. M. J. 2012, *ApJ*, 758, 57
- Lodieu, N., Béjar, V. J. S., & Rebolo, R. 2013, *A&A*, 550, L2
- Lucas, P. W., Tinney, C. G., Burningham, B., et al. 2010, *MNRAS*, 408, L56
- Luhman, K. L. 2014, *ApJ*, 786, L18
- Luhman, K. L., Burgasser, A. J., & Bochanski, J. J. 2011, *ApJ*, 730, L9
- Luhman, K. L., Burgasser, A. J., Labbé, I., et al. 2012, *ApJ*, 744, 135
- Marsh, K. A., Wright, E. L., Kirkpatrick, J. D. et al. 2013, *ApJ*, 762, 119
- Morley, C. V., Fortney, J. J., Marley, M. S., et al. 2012, *ApJ*, 756, 172
- Morley, C. V., Marley, M. S., Fortney, J. J., et al. 2014, *ApJ*, 787, 78
- Pinfield, D. J., Gromadzki, M., Leggett, S. K., et al. 2014, *MNRAS*, in press
- Saumon, D., & Marley, M. S. 2008, *ApJ*, 689, 1327
- Saumon, D., Marley, M. S., Abel, M., Frommhold, L., & Freedman, R. S. 2012, *ApJ*, 750, 74
- Simons, D. A., & Tokunaga, A. 2002, *PASP*, 114, 169
- Subasavage, J. P., Jao, W.-C., Henry, T. J., et al. 2009, *AJ*, 137, 4547
- Tinney, C. G., Faherty, J. K., Kirkpatrick, J. D., et al. 2012, *ApJ*, 759, 60
- Tokunaga, A. T., Simons, D. A., & Vacca, W. D. 2002, *PASP*, 114, 180
- Tokunaga, A. T., & Vacca, W. D. 2005, *PASP*, 117, 421
- Warren, S. J., Mortlock, D. J., Leggett, S. K., et al. 2007, *MNRAS*, 381, 1400
- Werner, M. W., Roellig, T. L., Low, F. J., et al. 2004, *ApJS*, 154, 1
- Wright, E. L., Eisenhardt, P. R. M., Mainzer, A. K., et al. 2010, *AJ*, 140, 1868

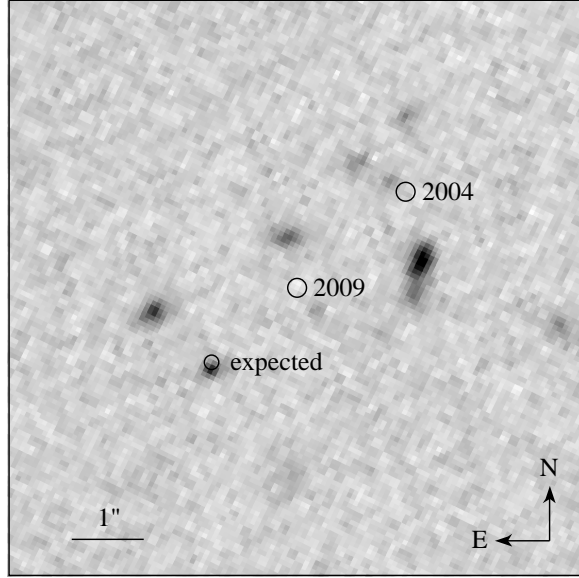


FIG. 1.— WFC3 F110W image of a  $8'' \times 8''$  field encompassing WD 0806-661 B. We have marked the positions of this object measured with *Spitzer* in 2004 and 2009 (Luhman et al. 2011) and the position expected in this image based on those earlier detections and the proper motion and parallax of the primary. A source is detected near the expected location, which we take to be WD 0806-661 B. The radius of each circle corresponds to  $1\sigma$ .

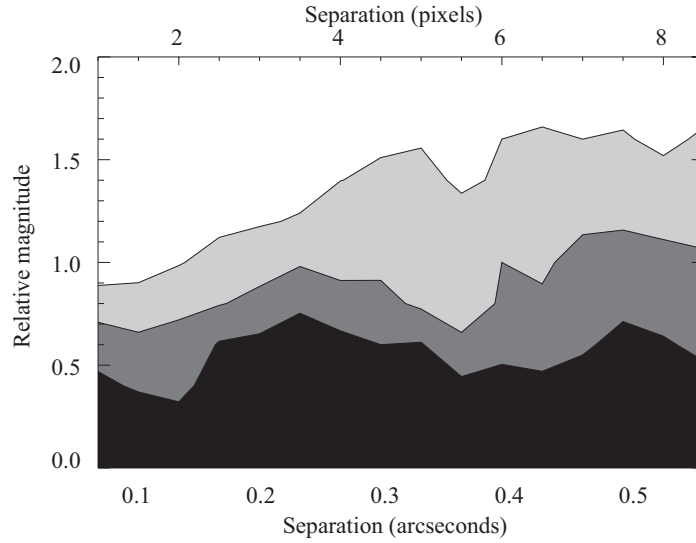


FIG. 2.— Relative magnitude limits at which 20%, 50%, and 80% (top to bottom) of simulated companions to WD 0806-661 B are recovered by our PSF analysis of the WFC3 F110W image.

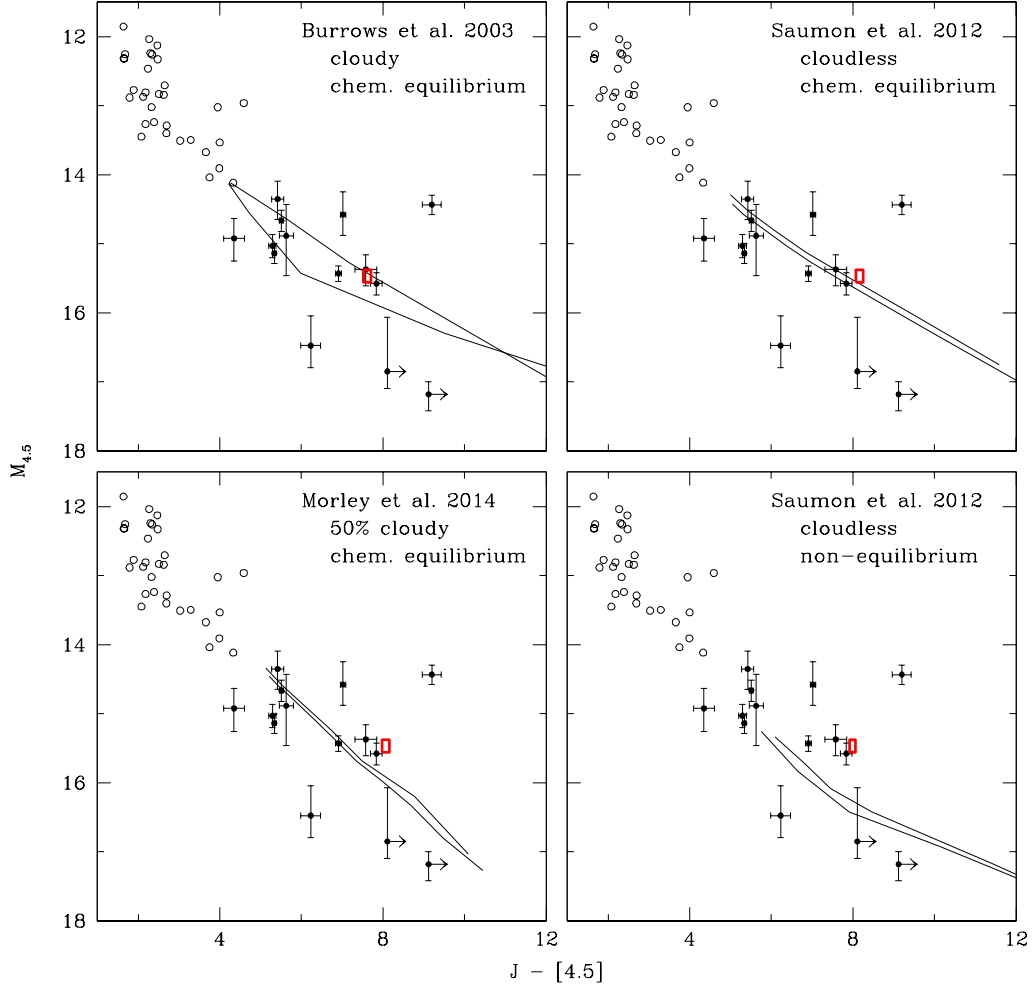


FIG. 3.— Color-magnitude diagrams for WD 0806-661 B (open rectangle) and samples of T dwarfs (open circles, Dupuy & Liu 2012, references therein) and Y dwarfs (filled circles with error bars, Cushing et al. 2011, 2014; Tinney et al. 2012; Beichman et al. 2013, 2014; Leggett et al. 2013; Marsh et al. 2013; Kirkpatrick et al. 2013; Dupuy & Kraus 2013; Luhman 2014). These data are compared to the magnitudes and colors predicted by four sets of models for ages of 1 and 3 Gyr (solid lines), which encompass the age of WD 0806-661 B ( $2 \pm 0.5$  Gy, Luhman et al. 2012).

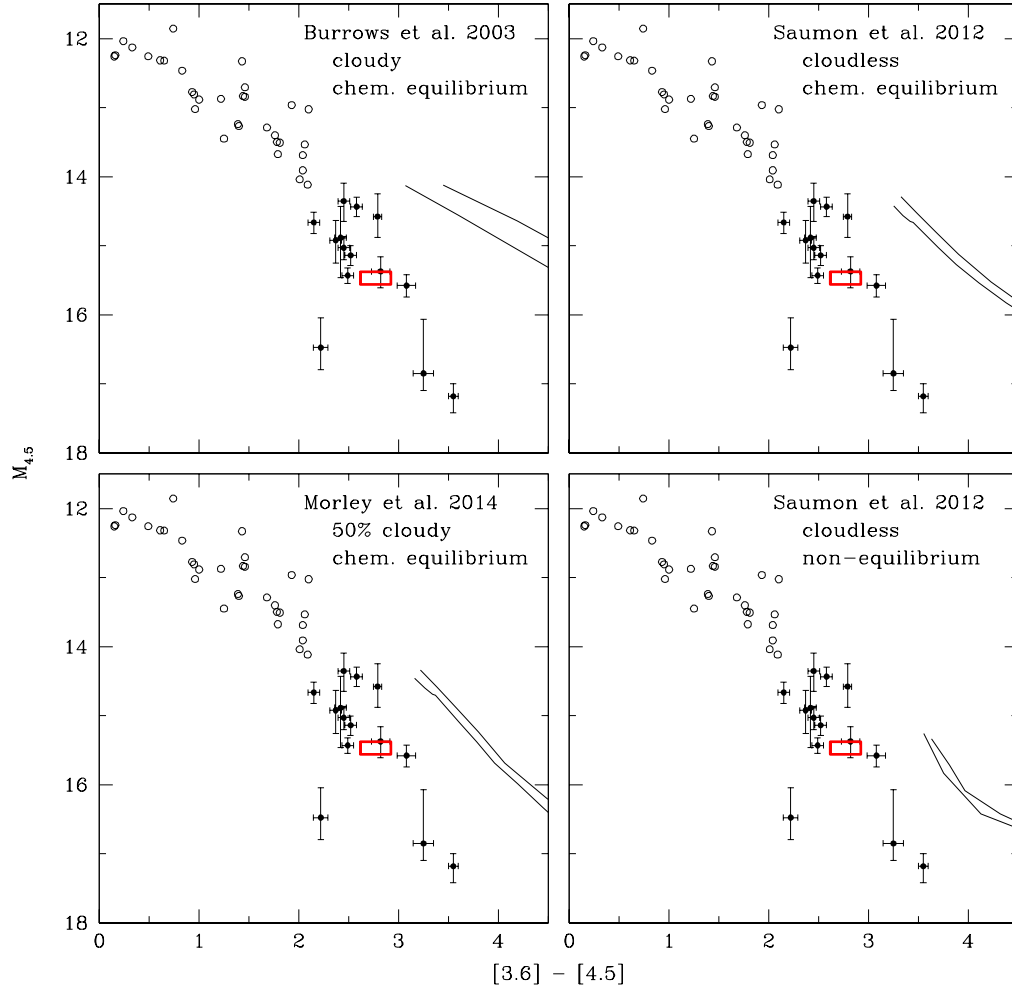


FIG. 4.— Same as Figure 3, except that the color is  $[3.6] - [4.5]$ .